Self-Assembling Process of Flash NanoPrecipitation in a Multi-Inlet Vortex Mixer (MIVM) to Produce Drug-Loaded Polymeric Nanoparticles

Hao Shen[1], Seungpyo Hong[2], Robert K. Prud'homme[3], and Ying Liu[1,2,*]

[1] *Department of Chemical Engineering, University of Illinois at Chicago, Chicago, IL 60607*

[2] *Department of Biopharmaceutical Sciences, University of Illinois at Chicago, Chicago, IL 60607*

[3] *Department of Chemical Engineering, Princeton University, Princeton, NJ 08544*

** To whom correspondence should be addressed.*

Email: liuying@uic.edu

Abstract

We present an experimental study of self-assembled polymeric nanoparticles in the process of Flash NanoPrecipitation using a Multi-Inlet Vortex Mixer (MIVM). β-carotene and polyethyleneimine (PEI) are used as a model drug and a macromolecule, respectively, and encapsulated in diblock copolymers. Flow patterns in the MIVM are microscopically visualized by mixing iron nitrate and potassium thiocyanate to precipitate $Fe(SCN)_x^{(3-x)+}$. Effects of physical parameters including Reynolds number, supersaturation rate, interaction force, and drug loading rate, on size distribution of the nanoparticle suspensions are investigated. It is critical for the nanoprecipitation process to have a short mixing time, so that the solvent replacement starts homogeneously in the reactor. The properties of the nanoparticles depend on the competitive kinetics of polymer aggregation and organic solute nucleation and growth. We report the existence of a threshold Reynolds number over which nanoparticle sizes become independent of mixing. A similar value of the threshold Reynolds number is confirmed by independent measurements of particle size, flow-pattern visualization, and our previous numerical simulation along with experimental study of competitive reactions in the MIVM.

Keywords *Reynolds number; supersaturation; competitive kinetics; nucleation and growth; micellization; micromixing*

Introduction

Nanoparticles have recently been the focus of much attention because of their broad biomedical applications in small molecule drug delivery (Cho et al. 2008; Johnson and Prud'homme 2003b; Liong et al. 2008), gene and protein delivery (Li et al. 2008; Ayame et al. 2008; Sun et al. 2008), medical imaging and diagnosis (Hainfeld et al. 2006; Xie et al. 2009), and photothermal therapy (Huang et al. 2006). Among the many nanoparticulate systems, polymeric nanoparticles self-assembled from amphiphilic block copolymers serve as promising drug carriers because of their unique hydrophobic core-hydrophilic shell structure. The hydrophilic domain forms the corona structure, giving the nanoparticles long blood circulation time and providing sustained release. The hydrophobic domain incorporated with hydrophobic drugs can increase the drug solubility and bioavailability. Self-directed localization of therapeutic agents to the disease-affected target tissue has been proposed to reduce side effects and toxicity. Achievements are particularly being made in the field of cancer chemotherapy, leading to increased survival rate (Sahoo et al. 2004). For tumor targeting, in addition to the ligand-receptor mediated uptake, passive drug accumulation at the tumor site based on the enhanced permeation and retention (EPR) effect is an important mechanism. The size of nanoparticles should be larger than 70 nm to prevent their rapid clearance due to renal filtration, but smaller than 300 nm to escape capture by phagocytic cells located in reticuloendothelial system (Kong et al. 2000). Highly monodispersed nanoparticles within the size range were reported to passively accumulate and to be retained at the tumor sites (Mitra et al. 2001).

Although research in the area has undergone rapid expansion in the last decade, most nanoparticles developed in research labs have not yet been applied in corresponding clinical treatments. One of the main reasons is the lack of control

over physical properties and surface functionality during mass production of nanomaterials. Many methods have been developed for the preparation of nanoparticles, such as supercritical processing (Tyrrell et al. 2009; Wang et al. 2004), two-step emulsification (Vauthier and Bouchemal 2009), sonication (Choi et al. 2010; Kumar et al. 2009), and nanoprecipitation (Fessi et al. 1989; Legrand et al. 2007; Thioune et al. 1997). However, they are all limited by major disadvantages. For example, although supercritical processing enables the production of pure drug compounds, it does not allow for control over surface properties of the particles. Emulsification of a compound followed by drying of the internal phase of the emulsion creates particles with polydispersity corresponding to the polydispersity of the original emulsion, which is generally broad. The drug loading depends on the partition coefficient of the drug into the hydrophobic core of the micelle, which means that the micelles always contain a minority of the drug compound (Kumar and Prud'Homme 2008). Reported values for the concentration of drug in the final micelle are from fractions of a percent to values of no more than 20 wt%, which is too low for most therapeutic uses (Kim and Lee 2001; Allen et al. 2000). Sonication has been used for producing micelles from drug-polymer conjugation. However, it must be followed by filtration to exclude the big aggregates, which reduces throughput and wastes a majority of the drug mass. Moreover, reproduction of active compounds needs to be further demonstrated for the conjugated drug. Finally, the nanoprecipitation method, first described by Fessi et al. (Fessi et al. 1989), is one of the easiest and most reproducible procedures to prepare nanoparticles. Nevertheless, direct nanoprecipitation in a traditional process results in heterogeneous mixing and a coupling of micromixing with nucleation and growth, resulting in polydispersed

particle sizes. At high drug concentrations it is generally not possible to limit particle growth to smaller than 200 nm (Horn and Rieger 2001).

Flash NanoPrecipitation, a scalable process to prepare nanoparticles with controlled size distribution and a high drug loading rate, was first proposed by Prud'homme (Johnson and Prud'homme 2003b) to produce polymeric nanoparticles encapsulating hydrophobic drugs. Three time scales are essentially important in the Flash NanoPrecipitation process: homogenous mixing time (τ_{mix}), polymer aggregation time (τ_{agg}), and organic solute nucleation and growth time ($\tau_{N.G.}$). The initial polymer aggregation and organic solute nucleation occur on much faster time scales than the mixing process. Therefore, the initial nanoparticle formation is mixing-limited. However, in the later stage, the kinetics of particle aggregation and growth becomes much slower, since the number concentration of the particles decreases rapidly and the hydrophilic block of the copolymer assembled on the surface of the particles provides steric stability. Eventually, as the aggregation number of the copolymer increases, the overall aggregation process is arrested and the nanoparticle is stabilized. Therefore, short mixing time ensures the solvent replacement starts homogeneously, so that the properties of the nanoparticles depend on the competitive kinetics of polymer aggregation and organic solute nucleation and growth. Rapid polymer aggregation results in the formation of dead micelles without any organic solute encapsulated inside, while rapid organic solute nucleation and growth results in undesired large particles.

A confined impinging jet (CIJ) mixer was developed for the process of FNP in one of our previous studies (Johnson and Prud'homme 2003a). The CIJ mixer provides rapid micromixing as fast as 1.5 milliseconds, but it requires equal momentum of the two inlet streams, which could cause rapid particle growth via

Ostwald ripening (Liu et al. 2007). To overcome the limitation of the CIJ mixer, a Multi-Inlet Vortex Mixer (MIVM) (Figure 1A) was developed by Liu and Prud'homme (Liu et al. 2008a). Use of the MIVM provides flexibility to introduce different compounds for formulation of nanoparticles with multiple active species, and also provides control over particle stability by allowing for the regulation of solvent/anti-solvent input ratios (Hoang et al. 2004; Lifshitz and Slyozov 1961; Liu et al. 2008a). Micromixing in the MIVM was characterized experimentally and numerically by using the competitive reactions of the acid-base reaction and DMP hydrolysis (Russ et al. 2010). The fluid dynamics in the MIVM was investigated using microscopic particle image velocimetry (micro-PIV) and computational fluid dynamics (CFD) (Cheng et al. 2009). The micro-PIV data were used to exhibit the velocity field and to evaluate the accuracy of CFD models in simulating the flow within the MIVM (Cheng et al. 2009). However, the physical parameters governing nanoparticle properties have not been presented by direct measurements on polymeric nanoparticles.

In this paper, we studied the fundamental mechanisms of self-assembly to produce nanoparticles using the MIVM. An amorphous copolymer poly(ethylene oxide)-*b*-poly(styrene) (PEO-*b*-PS), a semicrystalline copolymer poly(ethylene oxide)-*b*-poly(ε-caprolactone) (PEG-*b*-PCL), and an ionic copolymer poly(ethylene oxide)-*b*-poly(acrylic acid) (PEG-*b*-PAA) were used to produce nanoparticles encapsulating a small hydrophobic molecule, *β*-carotene, and cationic macromolecule, polyethyleneimine (PEI). The dependence of the nanoparticle sizes on Reynolds number, supersaturation rate, nature of polymers, drug loading rate, and the type of interaction forces was studied. Mixing patterns in the MIVM were imaged by a light microscope.

Experimental section

Materials

Poly(ethylene oxide)-*b*-poly(ε-caprolactone) (PEG-*b*-PCL) (Mw 5000-*b*-3600) and poly(ethylene oxide)-*b*-poly(acrylic acid) (PEG-*b*-PAA) (Mw 6000-*b*-2000) were purchased from Polymer Source (Dorval, Canada). Poly(ethylene oxide)-*b*-poly(styrene) (PEO-*b*-PS) (Mw 1000-*b*-3000) was kindly provided by Goldschmidt GmbH (Essen, Germany). *β*-carotene (95.0% purity), iodine, potassium iodide, tetrahydrofuran (THF), potassium thiocyanate, iron (III) nitrate and branched poly(ethyleneimine) (Mw 750,000) were purchased from Sigma-Aldrich (St Louis, MO). Unless otherwise stated, all chemicals were purchased at standard grades and used as received.

Mixing and flow pattern visualization

Iron nitrate and potassium thiocyanate were used to image the mixing process in the MIVM. The dimensions and the imaging area of the MIVM were shown in Figure 1. The reactor and channel height was 1.53 mm. The inlet channel width was 1.19 mm. The reactor diameter was 6.26 mm, and the outlet diameter was 1.40 mm. To observe flow patterns in the MIVM composed of dilute solutions and suspensions as the conditions of making nanoparticle suspensions, inorganic dyes were used instead of organic dyes. Organic dyes may affect the properties of aqueous solutions when dissolved at the concentrations sufficient for visualizing flow patterns in the MIVM (Tice et al. 2003). Digitally controlled syringe pumps (Harvard Apparatus, PHD 2000 programmable, Holliston, MA) were integrated with the MIVM to accurately control the flow rates of the inlet streams. The solution from stream 1 and stream 3 was 1 wt% iron nitrate dissolved in DI water.

The solution from stream 2 and stream 4 was 1 wt% potassium thiocyanate dissolved in DI water. Mixing of iron nitrate and potassium thiocyanate generated red precipitation of iron thiocyanate.

The four inlet streams had the same volumetric flow rate. Flow patterns in the center of the chamber, 6 mm in diameter, were observed under a microscope (American Scope, IN200A-P, Chino, CA) with an objective of 4x magnification and a digital microscope camera (Motic, Moticam 1000, Xiamen, China) coupled to an image analysis software (Motic images plus 2.0). The exposure time was 30 ms.

Nanoparticle preparation and characterization

Nanoparticles of β-carotene encapsulated in two block copolymers, PEO-*b*-PS (Mw 3000-*b*-1000) and PEG-*b*-PCL (Mw 5000-*b*-3600), were generated in the MIVM by hydrophobic interaction. For each copolymer used, stream 1 and 2 had the same volumetric flow rate. Stream 3 and 4 had the same volumetric flow rate, which was varied from 1 to 9 times the flow rate of stream 1 and 2 to obtain different supersaturation values. For nanoparticles of β-carotene encapsulated in PEO-*b*-PS (Mw 3000-*b*-1000), the solution from stream 1 was 1 wt% β-carotene dissolved in THF. The solution from stream 2 was 1 wt% PEO-*b*-PS (Mw 3000-*b*-1000) dissolved in THF. The other two streams were DI water. For nanoparticles of β-carotene encapsulated in PEG-*b*-PCL (Mw 5000-*b*-3600), the solution from stream 1 was PEG-*b*-PCL (Mw 5000-*b*-3600) with various concentrations from 1 wt% to 5 wt% and 1 wt% β-carotene dissolved in THF. The other three streams were DI water.

Nanoparticles of branched PEI (Mw 750,000) encapsulated in PEG-*b*-PAA (Mw 6000-*b*-2000) were generated in the MIVM by electrostatic interaction. The

solution from stream 1 was 1 wt% (or 2 wt%) PEG-*b*-PAA (Mw 6000-*b*-2000) dissolved in water. The solution from stream 2 was 0.43 wt% (or 0.86 wt%) PEI (Mw 750,000) dissolved in water. The concentration was designed to have equal positive and negative charges. The other two streams were DI water. The volumetric flow rates of stream 1 and stream 2 were kept equivalent. The volumetric flow rates of stream 3 and stream 4 were kept equivalent and four times of that of stream 1 and stream 2.

Nanoparticle sizes and size distribution were measured by dynamic light scattering (DLS) (Agilent, 7030 Nicomp DLS/ZLS-size and zeta, Santa Clara, CA). The particle sizes were reported as the intensity-weighted radius a_h, where $a_h \propto \sum_{k=1}^{\max,\infty} n_k a_k^6 \Big/ \sum_{k=1}^{\max,\infty} n_k a_k^5$. a_k was the radius of particle *k*, and n_k was the number of particles at a given size.

The images of the particles were taken by using a transmission electron microscope (TEM) (JEOL Ltd., JEM-3010, Tokyo, Japan) operated at 300 kV. The sample of β-carotene encapsulated in PEG-*b*-PCL was prepared by placing 30 microliters of the suspension on a formvar grid. After 30 minutes, 20 microliters of 2% phosphotungstic acid (PTA) (H_3PO_4 $12WO_3$ • $24H_2O$) (pH 6.9) was added to negatively stain the sample. Staining lasted for 2 minutes before PTA was removed by the filter paper. Detailed procedure of staining organic nanoparticles for TEM images can be found in the literature (Lavasanifar et al. 2001). The sample was dried for 4 hours before taking the TEM images. The images of β-carotene particles without protection of polymers were taken as a comparison to the nanoparticles. 30 microliters of the sample was placed on a membrane-coated carbon grid and dried for 4 hours prior to imaging. For both cases, the concentration of β-carotene was 0.1 wt%.

The encapsulation rate and drug loading rate (DLR) of β-carotene in block copolymers was characterized by sequential processes of filtration, freeze-drying, re-dissolving, and UV-Vis measurements. The encapsulation rate was calculated from the expression,

$$\text{Encapsulation rate}\,(\%) = \frac{\text{Amount of } \beta\text{-caroten encapsulated in nanoparticles}}{\text{Feeding amount of } \beta\text{-carotene}} \times 100\% .$$

The drug loading rate (DLR) was calculated from the expression,

$$DLR = \frac{mass \quad \beta - carotene \quad encapsulated}{total \quad mass \quad of \quad nanoparticles} \times 100\% .$$

The nanoparticles of β-carotene encapsulated in PEG-*b*-PCL were generated by using the MIVM and collected in a big reservoir of water (~100 times the dilution rate) to quench the reaction and prevent the fast growth of particle size due to Ostwald ripening. The nanoparticle suspensions were filtered through a 0.45 μm filter (VWR, 0.45 μm Polyethersulfone filter, West Chester, PA). β-carotene that was not encapsulated in the nanoparticles would form large crystals and be filtered out of the suspension. After the filtration, the nanoparticles were freeze-dried by using a freeze dryer (Labconco, FreeZone 6 liter console, Kansas City, MO) for 3 days. The nanoparticles were then re-dissolved in THF. The encapsulation rate and DLR of β-carotene was quantified by using a UV-Vis spectrophotometer (Beckman Coulter, DU800 UV/Visible spectrophotometer, Brea, CA). The absorbance was measured at a wavelength of 310 nm. Various drug loading rates were achieved by changing the weight ratio of β-carotene to PEG-*b*-PCL from 1:1 to 1:5.

Critical micelle concentration (CMC) measurements

Critical micelle concentration (CMC) of the diblock copolymers in water and THF mixed solvent was measured by using both the Baleux assay method (Baleux 1972) and the light scattering method (Johnson 2003). PEG-*b*-PCL was dissolved in water and THF mixed solvent and agitated by using a vortex mixer (Boekel, 270100 Tap Dancer-Vortex Mixer, Feasterville, PA). The concentration of PEG-*b*-PCL was much higher than the CMC of PEG-*b*-PCL to ensure the formation of PEG-*b*-PCL micelles. Solution of PEG-*b*-PCL in mixed solvent was pipetted into 100K Molecular Weight Cut Off centrifuge tubes (Pall, 100K Nanosep Centrifugal Devices, Port Washington, NY) and centrifuged by a centrifuge (Fisher Scientific, Marathon 16KM microcentrifuge, Pittsburgh, PA) at 14000G for 15 minutes. The concentration of PEG-*b*-PCL in the mixed solvent through the membrane after centrifuge was considered as the CMC. Iodine-potassium iodide solution was made of 0.03 grams of iodine and 0.06 grams of potassium iodide in 3 milliliters of DI water. The solution was kept in a brown glass bottle no longer than 8 days. 0.05 milliliters of the iodine-potassium iodide solution was then added to 2 milliliters of PEG-*b*-PCL solution. The light absorbance was measured by a UV-Vis spectrophotometer (Shimadzu, UV-1601, Kyoto, Japan) at a wavelength of 500 nm. The Baleux assay method was only used on the samples of THF to water ratio equal to or less than 10%, because at a higher THF ratio, the light absorbance was influenced by the organic solvent. The light scattering method (Johnson 2003) was also used to analyze the CMC of PEG-*b*-PCL in water and THF solvent mixture. Various concentrations of PEG-*b*-PCL in solvent mixture were prepared and the CMC was identified by the jump in light scattering when micelles formed.

Results and discussion

Effect of flow field and Reynolds number: Starting the competitive kinetics simultaneously

Flash NanoPrecipitation is a process of kinetic control instead of thermodynamic equilibrium which constrains the drug loading rate and causes broad size distribution and low stability as in most other processes, such as emulsion and traditional precipitation. At thermodynamic equilibrium, drug loading is driven by entropy of mixing of the drug with the hydrophobic core of the micelle. Based on Flory-Huggins theory and Chi mismatch, drug loading is disfavored (Ugelstad et al. 1992). The kinetic control of Flash NanoPrecipitation overcomes the drug loading limit.

High Reynolds number homogenous mixing was essential to start the competitive processes of organic solute nucleation and growth as well as polymer aggregation simultaneously and uniformly, which provided control over drug loading rate and uniform particle size distribution. However, the appropriate definition of Reynolds number is not obvious for a system with multiple inlet streams of solutions with various velocities, dimensions, and viscosities like the MIVM. Regression modeling on data from previous MIVM research was used to develop an optimal formulation of Reynolds number (*Re*) as (Russ et al. 2010),

$$\mathrm{Re} = \left[\sum_i \left(\frac{Q_{base}}{Q_{acid}} \right) \left(\frac{Q_i}{Q_{total}} \right) \mathrm{Re}_i^{2/3} \right]^{3/2} \qquad (1),$$

where $Q_{base,}$ $Q_{acid,}$ Q_{total}, and Q_i represented the total volumetric flow rate of the base streams, the acid streams, the total volumetric rate of all streams, and flow rate of stream *i*, respectively. Re_i was the Reynolds number of the *ith* inlet stream calculated by the average velocity, viscosity, and dimension of the inlet stream.

However, to be comparable to our previous simulation and experimental results, we kept the definition of *Re* in this study as,

$$\mathrm{Re} = \sum_{i=1,N} V_i L / \nu_i \qquad (2),$$

where V_i was the velocity of the *ith* inlet stream, L was the chamber diameter, ν_i was the kinematic viscosity of the *ith* inlet stream, and N=4 was the number of inlet streams.

Flow patterns inside an MIVM at various *Re* were visualized by mixing the streams of $Fe(NO_3)_3$ with KSCN to form inorganic complex $Fe(SCN)_x^{(3-x)+}$ (x~3, absorption maximum λ_{max} ~ 480nm, extinction coefficient ε ~ 5×10^3 $cm^{-1}\cdot M^{-1}$). The inorganic dye was chosen because of its Newtonian behavior. The viscosity of the solution of the complex was 1.08±0.05 mPa·s at the imaging concentration (<0.067 M) (Tice et al. 2003). The viscosity of the two colorless streams of $Fe(NO_3)_3$ (<0.067 M) and KSCN (<0.2 M) was 1.00±0.05 mPa·s (Tice et al. 2003). At the mixing front, the red precipitation of iron complex $Fe(SCN)_x^{(3-x)+}$ indicated the streamlines. With higher *Re*, flow had more circulation and streamlines were closer. Eventually diffusion across the streamlines was fast enough to make the mixing in the MIVM homogeneous. At low *Re*, the mixing time, τ_{mix}, was given by,

$$\tau_{mix} = l^2 / 2D \qquad (3),$$

where D (m^2/s) was the diffusion constant and l was the striation length, the distance over which mixing could occur by diffusion. For a molecule with a diffusion constant of D=10^{-9} m^2/s, reducing l from 100 μm to 1 μm decreases τ_{mix} from 5 s to 0.5 ms. The images showed that increasing *Re* enhanced mixing by reducing the striation length. At *Re* over 1400, the red precipitation of

$Fe(SCN)_x^{(3-x)+}$ is homogenous in the mixer under the microscope. Our previous results from numerical simulation and experimental analysis using competitive reactions revealed that adequate micromixing was obtained with *Re* over 1600 (Liu et al. 2008a).

The nanoparticle size dependence on *Re* is shown in Figure 2 and Figure 3. Similarly to our previous results from numerical simulation (Liu et al. 2008a), the transition happened at *Re* near 2000. With higher *Re*, the mixing was more homogeneous and effective. Over the critical *Re* (~2000), the flow was fully developed turbulence and the resulting particle sizes were not sensitive to the flow field. At low *Re* (*Re*<2000), in Figure 2A and 2B, nanoparticle sizes increased with the decrease of *Re*, while in Figure 3A, nanoparticle sizes decreased with the decrease of *Re*. This opposite transition was because of the different interaction forces between the encapsulated model drugs and diblock copolymers. The interaction between β-carotene and PEO-*b*-PS or PEG-*b*-PCL was hydrophobic interaction. The nanoparticle sizes depended on the competitive kinetics of polymer aggregation and β-carotene nucleation and growth. At lower *Re*, β-carotene and polymers were not homogeneously mixed, so that locally there were not sufficient polymers nearby to terminate the growth of β-carotene. Therefore the nanoparticle sizes were larger compared to the nanoparticles formed at higher *Re*. The interaction between positive charged PEI and negative charged PAA block of PEG-*b*-PAA is electrostatic interaction. At low *Re*, negative charged PEG-*b*-PAA had less chance to interact with positive charged PEI and nanoparticles were smaller compared to those generated at higher *Re*. At high *Re* (*Re*>2000), the MIVM provided adequate micromixing. Nanoparticle sizes no longer depended on *Re* or the flow field.

High *Re* homogeneous mixing was also critical for obtaining high drug encapsulation rate. The limited drug encapsulation from thermodynamic equilibrium could be discerned from the curves of solubility boundaries for organic solute and polymers as a function of anti-solvent addition (Figure 4). Figure 4 displays the solubility of *β*-carotene as a model hydrophobic drug and CMC of two diblock copolymers, PEO-*b*-PS and PEG-*b*-PCL, as a function of THF content at room temperature. Gradual anti-solvent addition involved traversing the operating line from the initially pure solvent condition to the intersection first with the solubility curve of *β*-carotene and then with the CMC curves of the diblock polymers as the stabilizer. At the point when the operating line crossed the solubility curve of *β*-carotene, *β*-carotene would begin to precipitate as unprotected crystals until more anti-solvent was added and polymers started aggregation. However, when the operating line intersected with the CMC curves of polymers, more than 70% of *β*-carotene had precipitated and grew to be large crystals, which would be filtered out of the suspension. Not only this was a waste of the active compound, but drug encapsulation rate in the nanoparticles was also low. In the process of Flash NanoPrecipitation, homogenous mixing could be reached in milliseconds to produce high levels of supersaturation for *β*-carotene as well as polymers at final solvent composition. The composition of the resulting nanoparticles was decided by the stoichiometry of the feeds instead of the partition coefficient of the drug with polymers. Therefore, polymeric nanoparticles with higher drug encapsulation rate were possible. When nanoparticles were generated at high *Re* in the MIVM, the encapsulation rate of *β*-carotene in block copolymers was higher than 85%.

Effects of supersaturation rate and nature of polymers

Supersaturation rate directly affected the nucleation and growth time of the organic solute and polymer aggregation time. The rate of nucleation, *J*, was estimated by the primary homogeneous nucleation rate (Dirksen and Ring 1991),

$$J \propto \exp\left[-\frac{16\pi\gamma^3\upsilon^2}{3k_B^3T^3(\ln S)^2}\right] \qquad (4),$$

where γ was solid-liquid interfacial tension and υ was molar volume of the solute. *S* was the supersaturation ratio defined as,

$$S = c(r)/c^* \qquad (5),$$

where $c(r)$ denoted the solubility of a particle with radius *r* and c^* was the equilibrium solubility. The rate for primary homogenous nucleation was derived by assuming that, for supersaturated solutions, solute molecules combined to produce embryos. Quasi-equilibrium developed between molecules and embryos, with a corresponding distribution of free energy due to the formation of a new volume and new surfaces. The nucleation rate calculated from equation 4 could be orders of magnitude different from experimentally measured rates, but the derivation captured the general features of particle formation (Dirksen and Ring 1991). By adopting homogeneous primary nucleation kinetics, the rate of block copolymer self-assembly was approximated by using equation 4 and inserting the value for supersaturation, *S*, defined as the ratio of polymer concentration over CMC. However, most primary nucleation in practice was likely to be heterogeneous nucleation, since supersaturation for homogeneous nucleation was much higher than heterogeneous nucleation. Heterogeneous nucleation could be estimated by using the same equation, but the surface energy of the solid-liquid interface was replaced by the surface energy of the solid-foreign surface interface.

There are two proposed mechanisms to explain the effects of supersaturation on size distributions of organic particles protected by block copolymers. In one scenario, nucleation started as homogeneous nucleation of β-carotene, since β-carotene had higher supersaturation rate and therefore higher nucleation rate. Polymers then began to assemble on the surfaces of the particles and finally arrested the particle growth. In another scenario, hydrophobic sites on the polymers could have served as the nucleation seeds. Nucleation then started as heterogeneous nucleation, and particle growth stopped when polymer aggregation was terminated by the combined effects of particle dilution and steric hindrance of the hydrophilic block of the copolymer. With either mechanism, at higher supersaturation, more nucleation sites were generated and nanoparticles were smaller.

In this study, β-carotene and diblock copolymers were dissolved in THF and mixed with DI water as an anti-solvent. Different supersaturation rates were generated by varying the ratio of THF and DI water. In experiments, by varying THF and water ratio from 1:1 v/v to 1:5 v/v, the supersaturation was changed more than 100 times for β-carotene (from 12 to 1489). However, supersaturation rates for PEO-*b*-PS and PEG-*b*-PCL remained at about 20 and 5, respectively. Regardless of *Re*, nanoparticles of 50 nm to 500 nm could be produced by changing supersaturation rates (Figure 2A and 2B). Further models and experiments need to be developed to determine whether the dependence of nanoparticle properties on supersaturation rate is through nucleation kinetics of the organic solute or polymer assembly.

The long-term stability of the nanoparticles depended on polymer nature and solvent composition. At the same supersaturation rate of β-carotene, nanoparticles

protected by PEO-*b*-PS were smaller than those protected by PEG-*b*-PCL (Figure 2A and 2B). Extensive studies (Mao et al. 2006; Kwon 2003; Lin et al. 2003; Photos et al. 2003; Mosqueira et al. 2001; Lee et al. 1999) have confirmed that the density of the coverage and the chain length of PEG influence the stability of the nanoparticles. In general, a longer PEG chain provides a higher energy barrier to prevent nanoparticles from coagulation and degradation. A recent study also found that the hydrophobic core may also affect the long-term stability of the nanoparticles (Monkenbusch et al. 2000). Stability of PEO-*b*-PS nanoparticles encapsulating hydrophobic compounds has been discussed and reported in the literature (Mullin 1993; Liu et al. 2007). PCL, which is biocompatible and biodegradable, has many applications in drug delivery (Geng and Discher 2005; Shuai et al. 2004b; Shuai et al. 2004a). However, the instability of PEG-*b*-PCL micelles and nanoparticles has been observed. One proposed mechanism was that low *Tg* PCL chains were sufficiently mobile on the surface and they could rearrange and begin to crystallize (Monkenbusch et al. 2000). The lamella morphology of PCL crystal phase would allow aggregation into larger lamella structures. Further studies will be required to unambiguously explain the instability observed in many PEG-*b*-PCL nanoparticle systems.

Solvent composition affected long-term stability of nanoparticle suspensions by Ostwald ripening (Mullin 1993; Liu et al. 2007). The diffusion-controlled growth kinetics was given by (Mullin 1993; Liu et al. 2007),

$$\frac{dr}{dt} = \frac{\gamma \upsilon^2 D_{drug} c^{\infty}}{3RTr^2} \qquad (6),$$

where D_{drug} and c^{∞} represented the diffusivity and bulk equilibrium solubility of the organic solute in the solution, respectively, and *r* was the particle radius. Bulk solubility of the organic solute increased exponentially with linear increase of

solvent concentration. Therefore, with higher solvent concentration, nanoparticles grew faster to be out of the nano-range. It was suggested that solvent had to be removed from the suspension quickly by flash solvent evaporation (Kumar and Prud'homme 2009) or dialysis.

Effect of drug loading rates

The dependence of particle size on DLR was measured by using PEG-*b*-PCL nanoparticles encapsulating β-carotene, with results presented in Figure 5. It was not surprising to find that nanoparticle diameters increased with higher DLR. At higher DLR, β-carotene nucleation and growth were relatively faster compared to the polymer micellization. Before the polymer arrested the growth of the particles, they had more time to become bigger. Figure 5 shows that with no drug encapsulated in the nanoparticles, as indicated by the intersection of the linearly extrapolated curve with y-axis, radius of the nanoparticles was 9 nm, which is consistent with the size of PEG-*b*-PCL micelles (Figure 2C). It is more interesting that the dependence of particle size on DLR was linear, which is consistent with our previous study on bifenthrin nanoparticles (Liu et al. 2008b). We are conducting more experiments and simulations to explain the linear relationship of particle size and DLR.

Conclusions

This study demonstrated the fundamental mechanisms of self-assembly to produce nanoparticles using a multi-inlet vortex mixer (MIVM). It provided a method to better design optimized nanoparticles for biomedical applications such as drug delivery and bioimaging. The MIVM was able to provide rapid micromixing and high supersaturation values to produce nanoparticles with

controlled size distribution and high drug loading rate. Nanoparticles of 50 nm to 500 nm were produced using the MIVM described in this paper.

Dependence of nanoparticle sizes on Reynolds number, supersaturation value, nature of polymers, drug loading rate, and type of interaction forces was characterized. High *Re* homogenous mixing was essential to start the competitive kinetics simultaneously and uniformly, which contributes to the formation of nanoparticles with controlled size distribution and high drug loading rate. Regardless of the definition of *Re*, there existed a threshold value, over which nanoparticle sizes were independent of *Re*. Microscopic images showed the transition of mixing patterns in the MIVM with the increase of *Re*. At high *Re* over 1400, diffusion across the streamlines was fast enough compared to the striation length so that we could not differentiate the separate streamlines indicated by the red precipitation of $Fe(SCN)_x^{(3-x)+}$. This result was close to our previous numerical simulation and experimental results which revealed that adequate micromixing was obtained with *Re* over 1600 (Liu et al. 2008a). The transition *Re* indicated by imaging was slightly smaller than the one indicated by simulation results and other experimental measurements, because determination of homogenous mixing by imaging was limited by microscope resolution. With a larger magnification and shorter exposure time, the transition *Re* might further agree with the number found in our other studies. Despite the small discrepancy in the transition *Re*, it was suggested that all the drug loaded polymeric nanoparticles should be prepared at high *Re* over the threshold value. At low *Re*, the nanoparticle sizes either decreased or increased with the increase of *Re*, determined by the interaction forces of the self-assembling process. Further investigation is required to understand the process of nanoparticle formation when the system is composed of multiple compounds.

The solubility curve of the organic compound and the CMC curves of the polymers elucidated that in order to have high drug encapsulation rate, spontaneous mixing to reach high supersaturation rate was necessary. Traditional nanoprecipitation by hand mixing, titration, or dialysis could not achieve high drug encapsulation rate, since anti-solvent was slowly added to the system and a significant amount of organic solute precipitated out of solution before the polymers started to form micelles.

The supersaturation level played a key role in governing the size of nanoparticles encapsulating hydrophobic organic compounds in amphiphilic block copolymers. At higher supersaturation, with higher nucleation rate, more nucleation sites were generated and nanoparticles were smaller.

In this study, we demonstrated that the MIVM can be utilized for encapsulation of a wide spectrum of materials spanning from model drugs such as β-carotene to hydrophilic charged polymers such as PEI, at a very high encapsulation efficiency. Further studies on encapsulating other therapeutic molecules need to be accomplished to demonstrate the advantages of a MIVM for generating polymeric nanoparticles. The linear relationship of the drug loading rate (DLR) and nanoparticle size also needs further investigation.

Acknowledgement

We thank Dr. Hayat Onyuksel at University of Illinois at Chicago for providing Dynamic Light Scattering for the measurements of nanoparticle sizes.

Figures

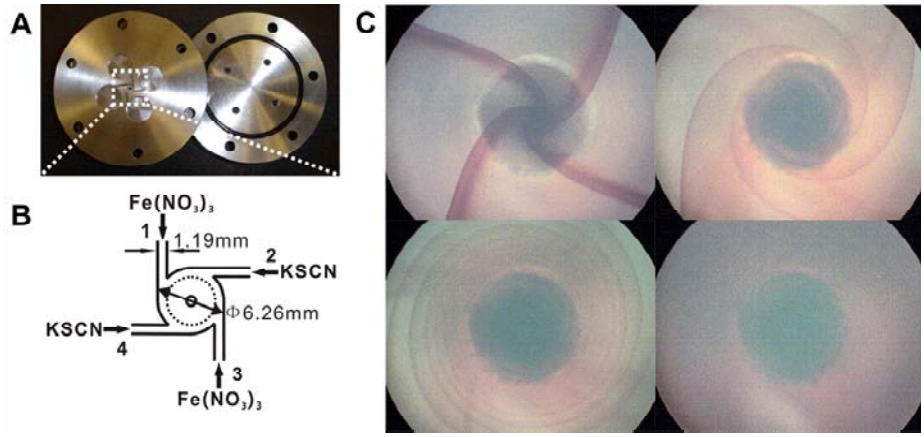

Fig. 1 Design of a multi-inlet vortex mixer (MIVM) and images of mixing and flow patterns in the MIVM. (A) Photo of the MIVM. (B) Diagram of the reaction center of the MIVM with four tangential inlet streams for flow-pattern visualization. (C) Microphotographs of mixing and flow patterns in the MIVM. Imaging area was indicated by dashed circle in (B). Mixing of $Fe(NO_3)_3$ and KSCN generated red precipitation of $Fe(SCN)_x^{(3-x)+}$ (x~3) complexes. Mixing patterns depended on Reynolds number (*Re*). Clockwise from the upper left image in (C), *Re* was increased. (Upper left: *Re*=267. Upper right: *Re*=537. Lower left: *Re*=806. Lower right: *Re*=1343.)

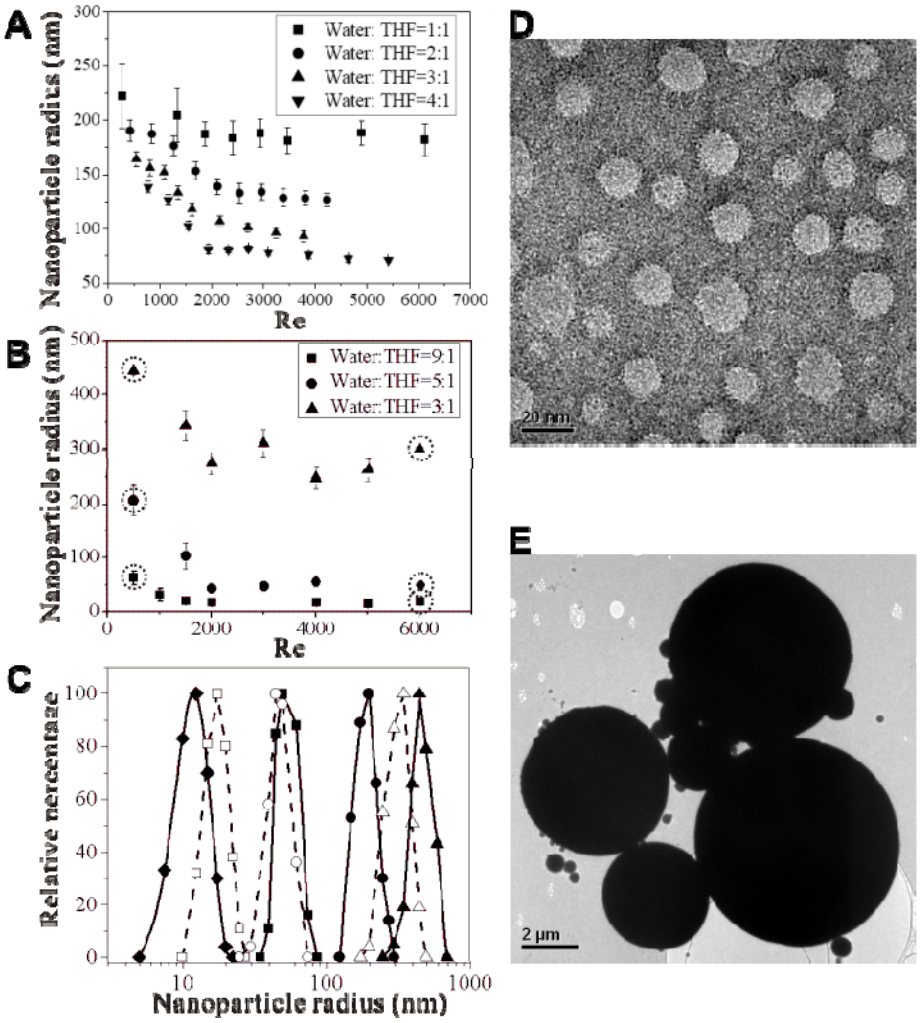

Fig. 2 The dependence of nanoparticle size on *Re*, and supersaturation rate. (A) Sizes of PEO-*b*-PS nanoparticles encapsulating *β*-carotene. (B) Sizes of PEG-*b*-PCL nanoparticles encapsulating *β*-carotene. (C) Size distributions of PEG-*b*-PCL micelles and nanoparticles encapsulating *β*-carotene. The solid diamonds for the first curve in (C) indicate the size distribution of PEG-*b*-PCL micelles. The remaining six curves show the size distributions of PEG-*b*-PCL nanoparticles encapsulating *β*-carotene, which correspond to the six conditions circled in (B) with the same symbol shapes. Hollow symbols in (C) denote that particles were generated at *Re*=6000, while solid symbols denote that particles were generated at *Re*=500. (D) The TEM image of *β*-carotene nanoparticles encapsulated in PEG-*b*-

PCL generated at *Re*=6000. The scale bar represents 20nm. (E) The TEM image of *β*-carotene particles generated from direct precipitation without polymer protection. The scale bar represents 2 μm.

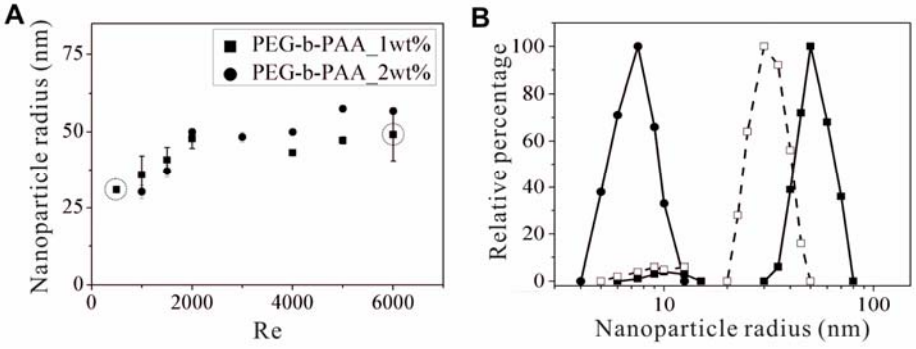

Fig. 3 Sizes of PEI and PEI/PEG-*b*-PAA complexes. (A) Sizes of the PEI/PEG-*b*-PAA complexes versus *Re*. (B) Size distributions of PEI and PEI/PEG-*b*-PAA complexes. -●- PEI, -□- PEI/PEG-*b*-PAA complexes produced at *Re*=500, and -■- PEI/PEG-*b*-PAA complexes produced at *Re*=6000.

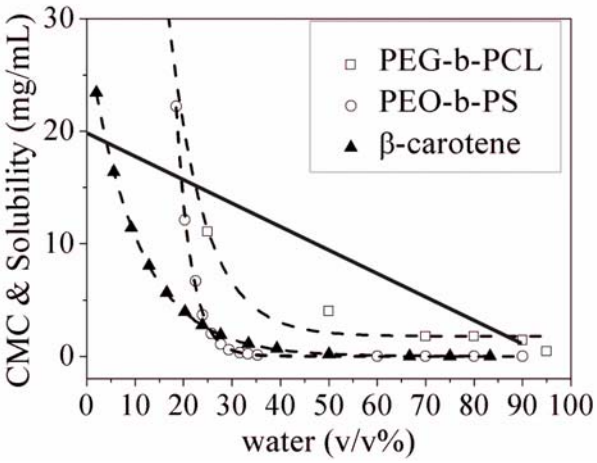

Fig. 4 Solubility of *β*-carotene, CMC of PEO-*b*-PS (MW 3000-*b*-1000) (measured by Johnson and Prud'homme) and CMC of PEG-*b*-PCL (MW 5000-*b*-3600). The

straight line represents the operating line for adding anti-solvent to a solution initially with 20 mg/mL β-carotene and 20 mg/mL of block copolymers.

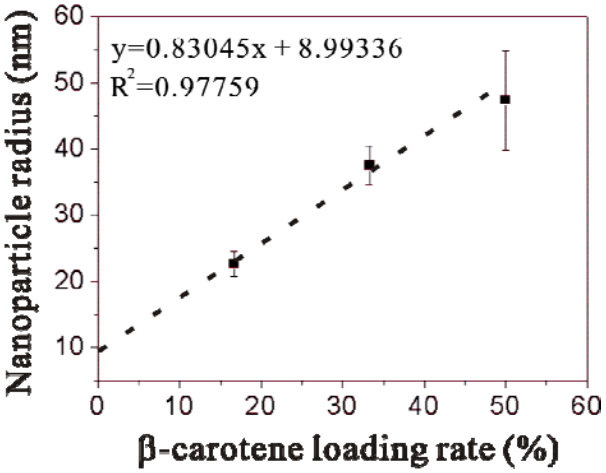

Fig. 5 The dependence of nanoparticle sizes on drug loading rate. Nanoparticles of β-carotene encapsulated in PEG-*b*-PCL were produced at *Re*=3225. The ratio of THF to water was 1:9 v/v. Prior to mixing, the concentration of β-carotene in THF was kept 1 wt% and concentrations of PEG-*b*-PCL were changed to be 1 wt%, 2 wt%, and 5 wt% to achieve various drug loading rates.

Reference

Allen C, Eisenberg A, Mrsic J, Maysinger D (2000) Pcl-b-peo micelles as a delivery vehicle for fk506: Assessment of a functional recovery of crushed peripheral nerve. Drug Delivery 7 (3):139-145

Ayame H, Morimoto N, Akiyoshi K (2008) Self-assembled cationic nanogels for intracellular protein delivery. Bioconjugate Chemistry 19 (4):882-890. doi:10.1021/bc700422s

Baleux B (1972) Colorimetric determination of nonionic polyethylene oxide surfactants using an iodine-iodide solution. CR Acad Sci Ser C 279:1617-1620

Cheng JC, Olsen MG, Fox RO (2009) A microscale multi-inlet vortex nanoprecipitation reactor: Turbulence measurement and simulation. Applied Physics Letters 94 (20):3. doi:204104
10.1063/1.3125428

Cho KJ, Wang X, Nie SM, Chen Z, Shin DM (2008) Therapeutic nanoparticles for drug delivery in cancer. Clinical Cancer Research 14 (5):1310-1316

Choi KY, Chung H, Min KH, Yoon HY, Kim K, Park JH, Kwon IC, Jeong SY (2010) Self-assembled hyaluronic acid nanoparticles for active tumor targeting. Biomaterials 31 (1):106-114

Dirksen JA, Ring TA (1991) Fundamentals of crystallization - kinetic effects on particle-size distributions and morphology. Chemical Engineering Science 46 (10):2389-2427

Fessi H, Puisieux F, Devissaguet JP, Ammoury N, Benita S (1989) Nanocapsule formation by interfacial polymer deposition following solvent displacement. International Journal of Pharmaceutics 55 (1):R1-R4

Geng Y, Discher DE (2005) Hydrolytic degradation of poly(ethylene oxide)-block-polycaprolactone worm micelles. Journal of the American Chemical Society 127 (37):12780-12781. doi:10.1021/ja053902e

Hainfeld JF, Slatkin DN, Focella TM, Smilowitz HM (2006) Gold nanoparticles: A new x-ray contrast agent. British Journal of Radiology 79 (939):248-253. doi:10.1259/bjr/13169882

Hoang TKN, Deriemaeker L, La VB, Finsy R (2004) Monitoring the simultaneous ostwald ripening and solubilization of emulsions. Langmuir 20 (21):8966-8969

Horn D, Rieger J (2001) Organic nanoparticles in the aqueous phase - theory, experiment, and use. Angewandte Chemie-International Edition 40 (23):4331-4361

Huang XH, El-Sayed IH, Qian W, El-Sayed MA (2006) Cancer cell imaging and photothermal therapy in the near-infrared region by using gold nanorods. Journal of the American Chemical Society 128 (6):2115-2120. doi:10.1021/ja057254a

Johnson BK (2003), Princeton University, Princeton

Johnson BK, Prud'homme RK (2003a) Chemical processing and micromixing in confined impinging jets. Aiche Journal 49 (9):2264-2282

Johnson BK, Prud'homme RK (2003b) Flash nanoprecipitation of organic actives and block copolymers using a confined impinging jets mixer. Australian Journal of Chemistry 56:1021-1024. doi:10.1071/ch03115

Kim SY, Lee YM (2001) Taxol-loaded block copolymer nanospheres composed of methoxy poly(ethylene glycol) and poly(epsilon-caprolactone) as novel anticancer drug carriers. Biomaterials 22 (13):1697-1704

Kong G, Braun RD, Dewhirst MW (2000) Hyperthermia enables tumor-specific nanoparticle delivery: Effect of particle size. Cancer Research 60 (16):4440-4445

Kumar V, Prud'Homme RK (2008) Thermodynamic limits on drug loading in nanoparticle cores. Journal of Pharmaceutical Sciences 97 (11):4904-4914

Kumar V, Prud'homme RK (2009) Nanoparticle stability: Processing pathways for solvent removal. Chemical Engineering Science 64 (6):1358-1361

Kumar V, Wang L, Riebe M, Tung HH, Prud'homme RK (2009) Formulation and stability of ltraconazole and odanacatib nanoparticles: Governing physical parameters. Molecular Pharmaceutics 6 (4):1118-1124. doi:10.1021/mp900002t

Kwon GS (2003) Polymeric micelles for delivery of poorly water-soluble compounds. Critical Reviews in Therapeutic Drug Carrier Systems 20 (5):357-403

Lavasanifar A, Samuel J, Kwon GS (2001) Micelles self-assembled from poly(ethylene oxide)-block-poly(n-hexyl stearate l-aspartamide) by a solvent evaporation method: Effect on the solubilization and haemolytic activity of amphotericin b. Journal of Controlled Release 77 (1-2):155-160

Lee LS, Conover C, Shi C, Whitlow M, Filpula D (1999) Prolonged circulating lives of single-chain fv proteins conjugated with polyethylene glycol: A comparison of conjugation chemistries and compounds. Bioconjugate Chemistry 10 (6):973-981

Legrand P, Lesieur S, Bochot A, Gref R, Raatjes W, Barratt G, Vauthier C (2007) Influence of polymer behaviour in organic solution on the production of polylactide nanoparticles by nanoprecipitation. International Journal of Pharmaceutics 344:33-43. doi:10.1016/j.ijpbarm.2007.05.054

Li SD, Chen YC, Hackett MJ, Huang L (2008) Tumor-targeted delivery of sirna by self-assembled nanoparticles. Molecular Therapy 16 (1):163-169. doi:10.1038/sj.mt.6300323

Lifshitz IM, Slyozov VV (1961) The kinetics of precipitation from supersaturated solid solutions. Journal of Physics and Chemistry of Solids 19 (1-2):35-50

Lin WJ, Juang LW, Lin CC (2003) Stability and release performance of a series of pegylated copolymeric micelles. Pharmaceutical Research 20 (4):668-673

Liong M, Lu J, Kovochich M, Xia T, Ruehm SG, Nel AE, Tamanoi F, Zink JI (2008) Multifunctional inorganic nanoparticles for imaging, targeting, and drug delivery. Acs Nano 2 (5):889-896. doi:10.1021/nn800072t

Liu Y, Cheng CY, Prud'homme RK, Fox RO (2008a) Mixing in a multi-inlet vortex mixer (mivm) for flash nano-precipitation. Chemical Engineering Science 63 (11):2829-2842. doi:10.1016/j.ces.2007.10.020

Liu Y, Kathan K, Saad W, Prud'homme RK (2007) Ostwald ripening of beta-carotene nanoparticles. Physical Review Letters 98 (3). doi:036102
10.1103/PhysRevLett.98.036102

Liu Y, Tong Z, Prud'homme RK (2008b) Stabilized polymeric nanoparticles for controlled and efficient release of bifenthrin. Pest Management Science 64 (8):808-812. doi:10.1002/ps.1566

Mao SR, Neu M, Germershaus O, Merkel O, Sitterberg J, Bakowsky U, Kissel T (2006) Influence of polyethylene glycol chain length on the physicochemical and biological properties of poly(ethylene imine)-graft-poly(ethylene glycol) block copolymer/sirna polyplexes. Bioconjugate Chemistry 17 (5):1209-1218. doi:10.1021/bc060129j

Mitra S, Gaur U, Ghosh PC, Maitra AN (2001) Tumour targeted delivery of encapsulated dextran-doxorubicin conjugate using chitosan nanoparticles as carrier. Journal of Controlled Release 74:317-323

Monkenbusch M, Schneiders D, Richter D, Willner L, Leube W, Fetters LJ, Huang JS, Lin M (2000) Aggregation behaviour of pe-pep copolymers and the winterization of diesel fuel. Physica B-Condensed Matter 276:941-943

Mosqueira VCF, Legrand P, Morgat JL, Vert M, Mysiakine E, Gref R, Devissaguet JP, Barratt G (2001) Biodistribution of long-circulating peg-grafted nanocapsules in mice: Effects of peg chain length and density. Pharmaceutical Research 18 (10):1411-1419

Mullin JW (1993) Crystallization. 3rd edn. Butterworth Heinemann, Oxford, UK

Photos PJ, Bacakova L, Discher B, Bates FS, Discher DE (2003) Polymer vesicles in vivo: Correlations with peg molecular weight. Journal of Controlled Release 90 (3):323-334. doi:10.1016/s0168-3659(03)00201-3

Russ B, Liu Y, Prud'homme RK (2010) Optimized descriptive model for micromixing in a vortex mixer. Chemical Engineering Communications 197 (8)

Sahoo SK, Ma W, Labhasetwar V (2004) Efficacy of transferrin-conjugated paclitaxel-loaded nanoparticles in a murine model of prostate cancer. International Journal of Cancer 112 (2):335-340. doi:10.1002/ijc.20405

Shuai XT, Ai H, Nasongkla N, Kim S, Gao JM (2004a) Micellar carriers based on block copolymers of poly(e-caprolactone) and poly(ethylene glycol) for doxorubicin delivery. Journal of Controlled Release 98 (3):415-426. doi:10.1016/j.jconrel.2004.06.003

Shuai XT, Merdan T, Schaper AK, Xi F, Kissel T (2004b) Core-cross-linked polymeric micelles as paclitaxel carriers. Bioconjugate Chemistry 15 (3):441-448. doi:10.1021/bc034113u

Sun TM, Du JZ, Yan LF, Mao HQ, Wang J (2008) Self-assembled biodegradable micellar nanoparticles of amphiphilic and cationic block copolymer for sirna delivery. Biomaterials 29 (32):4348-4355. doi:10.1016/j.biomaterials.2008.07.036

Thioune O, Fessi H, Devissaguet JP, Puisieux F (1997) Preparation of pseudolatex by nanoprecipitation: Influence of the solvent nature on intrinsic viscosity and interaction constant. International Journal of Pharmaceutics 146 (2):233-238

Tice JD, Song H, Lyon AD, Ismagilov RF (2003) Formation of droplets and mixing in multiphase microfluidics at low values of the reynolds and the capillary numbers. Langmuir 19 (22):9127-9133. doi:10.1021/la030090w

Tyrrell Z, Winoto W, Shen YQ, Radosz M (2009) Block copolymer micelles formed in supercritical fluid can become water-dispensable nanoparticles: Poly(ethylene glycol)-block-poly(epsilon-caprolactone) in trifluoromethane. Industrial & Engineering Chemistry Research 48 (4):1928-1932. doi:10.1021/ie801472n

Ugelstad J, Berge A, Ellingsen T, Schmid R, Nilsen TN, Mork PC, Stenstad P, Hornes E, Olsvik O (1992) Preparation and application of new monosized polymer particles. Progress in Polymer Science 17 (1):87-161

Vauthier C, Bouchemal K (2009) Methods for the preparation and manufacture of polymeric nanoparticles. Pharmaceutical Research 26 (5):1025-1058. doi:10.1007/s11095-008-9800-3

Wang YL, Dave RN, Pfeffer R (2004) Polymer coating/encapsulation of nanoparticles using a supercritical anti-solvent process. Journal of Supercritical Fluids 28 (1):85-99. doi:10.1016/s0896-8446(03)00011-1

Xie JP, Zheng YG, Ying JY (2009) Protein-directed synthesis of highly fluorescent gold nanoclusters. Journal of the American Chemical Society 131 (3):888-+. doi:10.1021/ja806804u